

## From Differential Image Motion to Seeing

A. TOKOVININ

Cerro Tololo Inter-American Observatory, Casilla 603, La Serena, Chile; atokovinin@ctio.noao.edu

Received 2002 May 6; accepted 2002 June 8

**ABSTRACT.** The theory of the differential image motion monitor (DIMM), a standard and widely spread method of measuring astronomical seeing, is reviewed and extended. More accurate coefficients for computing the Fried parameter from the measured variance of image motion are given. They are tested by numerical simulations that show that any DIMM measures Zernike tilts, not image centroids as generally assumed. The contribution of CCD readout noise to image motion variance is modeled. It can substantially bias DIMM results if left unsubtracted. The second most important DIMM bias comes from the used exposure time, which is typically not short enough to freeze image motion completely. This effect is studied quantitatively for real turbulence and wind profiles, and its correction by interlaced short and long exposures is validated. Finally, the influence of turbulence outer scale reduces image size in large telescopes by 10% or more compared to the standard theory; new formulae to compute FWHM and half-energy diameter of the atmospheric point-spread function that take into account outer scale are provided.

### 1. INTRODUCTION

Ground-based astronomy is severely limited by the atmospheric optical turbulence, often called *seeing* (Young 1974). Much effort has been invested in the search for good sites and in studies of image quality at existing sites. With the advent of adaptive optics and interferometry, the importance of good seeing increases even more. A worldwide search for new sites with superb seeing is in progress for the next generation of extremely large telescopes (Andersen, Ardeberg, & Gilmozzi 1999).

Image degradation in the terrestrial atmosphere is broadly understood theoretically in the framework of the Kolmogorov turbulence model (Tatarskii 1961; Roddier 1981). In this model, a single parameter—typically Fried’s parameter  $r_0$  (Fried 1965)—is sufficient to describe all seeing effects. This parameter can be measured from the image motion in a small telescope.

The differential image motion monitor (DIMM) is now a universally accepted instrument for seeing measurements. The Fried parameter is estimated from the variance of the differential image motion in two small apertures, usually cut out in a single larger telescope pupil by a mask (Fig. 1). This approach has a practical advantage of being insensitive to shake and tracking errors, at least to first order.

The DIMM concept was introduced by Stock & Keller (1960). Its modern implementation is described by Sarazin & Roddier (1990) and Vernin & Muñoz-Tuñón (1995). Nowadays, many observatories build DIMMs using cheap CCD cameras and amateur telescopes. Without being exhaustive, I cite here Wood, Rodgers, & Russell (1995), Sagar et al. (2000),

Ehgamberdiev et al. (2000), and Boccas et al. (2000)<sup>1</sup> as proof of DIMM’s success and proliferation. I take parameters of the Cerro Tololo Inter-American Observatory (CTIO) DIMM (aperture diameter 6 cm, baseline 19 cm, CCD pixel size  $0''.77$ ) as representative for these instruments. A good theory of DIMMs was published by Martin (1987). This paper continues the work of Martin by considering additional effects.

The difference of the tilts over two DIMM subapertures is proportional to the second derivative of the wave front, or curvature. Thus, a DIMM is a form of curvature sensor. Another instrument to deduce seeing from wave-front curvature is described by Roddier, Graves, & Limburg (1990). On the other hand, the DIMM can be viewed as a Shack-Hartmann (S-H) sensor with only two apertures; extensive studies of these sensors are partially applicable to DIMMs (van Dam & Lane 2000; Irwan & Lane 1999). Other methods to measure  $r_0$  such as absolute image motion or the shearing interferometer (Dainty & Scaddan 1975; Roddier 1976) are not immune to pointing errors, making them unsuitable for use as robust site-testing instruments.

The DIMM’s success and widespread implementation has led to some confusion. A DIMM is often thought to be a robust and self-calibrated instrument that always measures the seeing correctly. However, a number of subtle instrumental effects in DIMMs do bias the results. As long as site comparison was based on identical instruments, their systematic errors were of secondary importance. Now there is a strong need to compare seeing measures obtained by teams using different equipment.

---

<sup>1</sup> M. Boccas et al. 2000, Description of CTIO DIMM, <http://www.ctio.noao.edu/telescopes/dimm/dimm.html>.

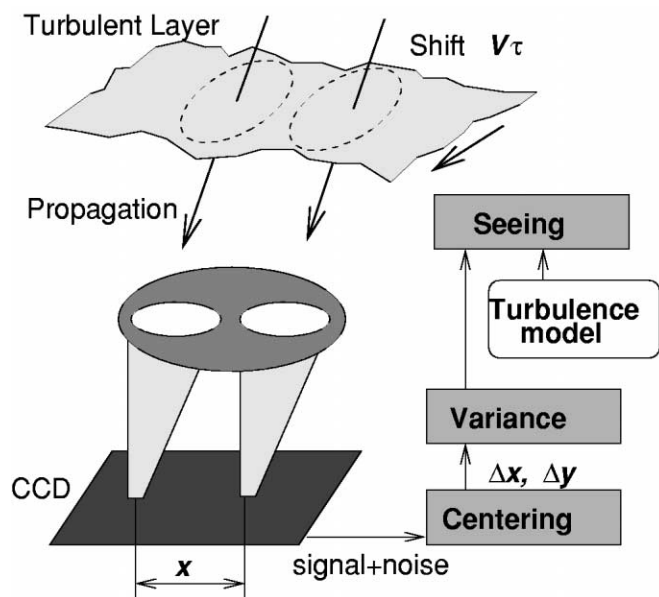


FIG. 1.—Differential image motion monitor (DIMM). Atmospherically distorted wave fronts are detected by two subapertures. The coordinates of the two images (spots) on short-exposure CCD frames are determined by some centering algorithm. The variance of the coordinate difference is used to compute the seeing with the help of a turbulence model. Instrumental effects that bias seeing measurements include propagation, shifts of wave fronts during exposure, CCD noise, centering method, and data reduction procedures.

Accurate calibration and debiasing of DIMM results becomes critical for site comparison and for prediction of telescope seeing.

Early comparisons of telescope seeing with “DIMM seeing” have shown their good agreement. Nowadays, the quality of large telescopes has increased significantly, and they are, generally, nearly free from both optical defects and locally generated seeing. Image quality in telescopes such as the VLT is sometimes found to be better than the “seeing” measured by a local DIMM, calling for a better interpretation of DIMM data. This article addresses the problem by taking into account both DIMM biases and the effects of turbulence outer scale.

The article is structured as follows. In § 2, I review the relation between differential image motion in DIMMs and the Fried parameter  $r_0$  within the framework of the standard (Kolmogorov) turbulence model and provide updated formulae for DIMM data reductions. In § 3, I show how to correct DIMM data for the two most important biases, finite exposure time and centroiding noise. This section contains the results of numerical simulations of DIMM operation. Then in § 4, the image size in large telescopes is addressed for the von Kármán turbulence model and an engineering formula to compute seeing is suggested to replace the standard (infinite-scale) relationship. The conclusions and practical recommendations are given in § 5. The Appendix gives additional insights into DIMM interactions with the atmospheric turbulence spectrum.

## 2. RELATIONSHIP BETWEEN DIFFERENTIAL IMAGE MOTION AND $r_0$

### 2.1. Centering Algorithms

The theory of the DIMM assumes that the centers of images formed by subapertures are defined as centers of gravity, also called centroids, G-tilts (Tyler 1994), or angle-of-arrival fluctuations. They are related to wave-front gradients averaged over subapertures. If  $I(x, y)$  is the light intensity distribution in a stellar image at the telescope focal plane (with background subtracted), its centroid in the  $x$ -direction,  $x_G$ , is defined to be

$$x_G = I_{\text{tot}}^{-1} \int xI(x, y) dx dy, \quad (1)$$

where  $I_{\text{tot}}$  is the total flux (the integral of image intensity). For a discrete (pixelized) CCD image, the integral is replaced by the sum over all pixels.

The centroid is the optimum position estimator for a Gaussian image profile that gives the lowest possible error for a perfect detector with only Poisson noise and zero readout noise (Irwin & Lane 1999). However, even for a perfect diffraction image, this is no longer the case because the intensity of image wings does not decrease fast enough. The readout noise contributes additional centroid error. Hence, it is not possible to compute *true* image centroids in either a DIMM or an S-H wave-front sensor.

Two centroiding methods, thresholding and windowing, are commonly used in practice. For *thresholding*, the integration (or summation) in equation (1) is extended only over pixels where  $I(x, y) > \gamma I_{\text{max}}$ , where  $I_{\text{max}}$  is the peak intensity in the image and  $\gamma$  is the relative threshold. There is an alternative way of thresholding: first, the threshold is subtracted from the image, then the centroid is computed for nonnegative pixels:

$$x_T = \frac{\sum_{I_{ij} > \gamma I_{\text{max}}} x_{ij} I'_{ij}}{\sum_{I_{ij} > \gamma I_{\text{max}}} I'_{ij}}, \quad (2)$$

where  $I'_{ij} = I_{ij} - \gamma I_{\text{max}}$ . This kind of thresholding reduces the weight of pixels in the image wings and is closer to an optimal fit.

In the *windowing* method, only the pixels within some radius from image center are taken into account. The center itself must be known, at least approximately. Usually, the coordinates  $x^*$ ,  $y^*$  of the brightest pixel are taken as window center. The centroid  $x_w$  is then

$$x_w = \frac{\sum_{\text{window}} x_{ij} I_{ij}}{\sum_{\text{window}} I_{ij}}. \quad (3)$$

The centering window can be of any shape, but here I consider only a circular window of radius  $r$ . It is reasonable to select  $r$  equal to the radius of the first dark ring in the Airy image,

$1.22\lambda/D$  rad, in order to minimize the effects of truncation at window border. The larger the window, the closer  $x_w$  will be to  $x_G$ .

Windowing and thresholding are similar: when there is no noise, cutting the image at some reasonable threshold is equivalent to cutting off image wings with a circular window, provided that the image has circular symmetry. Between those two methods, I prefer windowing because it leads to a simpler noise model (see below). Theoretically, the best way to estimate image position in the presence of noise would be to fit the expected image profile to the observed one. Our numerical simulations, however, show that the gain of fitting over thresholding or windowing with optimally chosen parameters is not dramatic, so here we do not consider fitting any further.

It is usually assumed that the shape of images in a DIMM is close to that of an Airy disk and that it does not change, in which case the various centering methods differ only in precision. This assumption is wrong. DIMMs often work in the regime  $D/r_0 \geq 1$  when atmospheric distortions within subapertures cannot be neglected. Astigmatism and defocus do not shift the spot centers, and the largest remaining term of random aberration is coma. In Figure 2, the image-center shifts produced by the different methods are plotted as a function of the coma coefficient  $a_6$ . The true centroid is a linear function of  $a_6$ , being simply proportional to the average wave-front gradient over aperture. But the other “centroids” react to coma much less and with opposite sign!

The maximum intensity of an aberrated image corresponds to that location in the field where the rms residual aberration is minimal. This location is found by the tilt of the least-squares fit plane, called Zernike tilt or Z-tilt (Tyler 1994; Sasiela 1994). In the numerical experiment shown in Figure 2, the Z-tilt remains zero. We see that windowing or thresholding is closer to Z-tilt than to centroid (G-tilt). *Therefore, image motion as measured in DIMMs corresponds to Z-tilts, not to G-tilts as generally believed.*

The difference between atmospheric G- and Z-tilts is small but far from negligible. For  $D/r_0 = 1$ , the rms coma coefficient is 0.08 rad. We see from Figure 2 that a 1 rad coma moves the G-centroid by  $0.8192\lambda/D$ , hence the difference between G- and Z-tilts approaches 0.1 at 10 cm apertures. This effect has been discovered by Vernin & Muñoz-Tuñón (1995) through numerical modeling; they called it “thresholding noise” and estimated its variance to be about 15% of the atmospheric differential image motion.

Thresholding noise cannot be quadratically subtracted from the measured variance of image motion because atmospheric coma is partially correlated with atmospheric tilts (Wang & Markey 1978). I explicitly take this effect into account by considering that a DIMM actually measures Z-tilts instead of G-tilts. With this modified definition of the DIMM signal, the thresholding noise disappears, but the theoretical formulae must be changed accordingly.

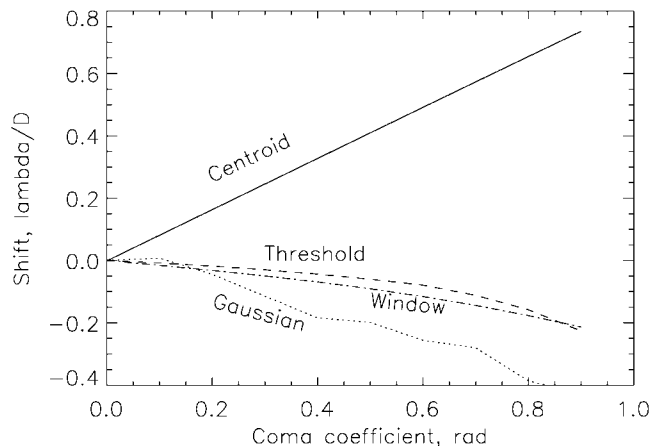


FIG. 2.—Displacement of the image center computed by different methods (without noise) as a function of the coma aberration. *Solid line*: true centroid; *dashed line*: thresholding with  $\gamma = 0.2$ ; *dash-dotted line*: windowing with  $r = 1.22\lambda/D$ ; *dotted line*: Gaussian fit.

## 2.2. Formulae for $r_0$

The formulae used to compute seeing from image motion variance are usually taken from Sarazin & Roddier (1990). Previous analyses were published by Fried (1975) and Martin (1987). The variance of the differential image motion  $\sigma_d^2$  (in square radians) is related to the Fried parameter  $r_0$ , the wavelength  $\lambda$  for which this parameter is given, and to the subaperture diameter  $D$  as

$$\sigma_d^2 = K\lambda^2 r_0^{-5/3} D^{-1/3}, \quad (4)$$

where all quantities are in the same units (meters) and  $K$  is a constant. It must be noted that the product  $\lambda^2 r_0^{-5/3}$  is independent of the wavelength  $\lambda$ . *Differential and absolute image motion is completely achromatic, and the response of the CCD, the stellar spectrum, etc., are irrelevant for seeing measurements.* This is why there are usually no spectral filters in DIMMs.

The FWHM  $\epsilon_0$  of the long-exposure seeing-limited point-spread function (PSF) in large telescopes is computed with the standard formula:

$$\epsilon_0 = \frac{0.98\lambda}{r_0} = 0.98 \left(\frac{D}{\lambda}\right)^{0.2} \left(\frac{\sigma_d^2}{K}\right)^{0.6}, \quad (5)$$

which is commented upon in § 4. Here  $\lambda$  is the imaging wavelength; it is well known that  $r_0 \propto \lambda^{6/5}$  and  $\epsilon_0 \propto \lambda^{-1/5}$ . It is common practice to express DIMM results as seeing in the sense of equation (5) (forgetting sometimes to specify at which wavelength this seeing was computed). Keeping this tradition, the DIMM seeing should be always interpreted this way. *I strongly suggest to adopt a wavelength of 0.5  $\mu\text{m}$  as standard for seeing data computation.*

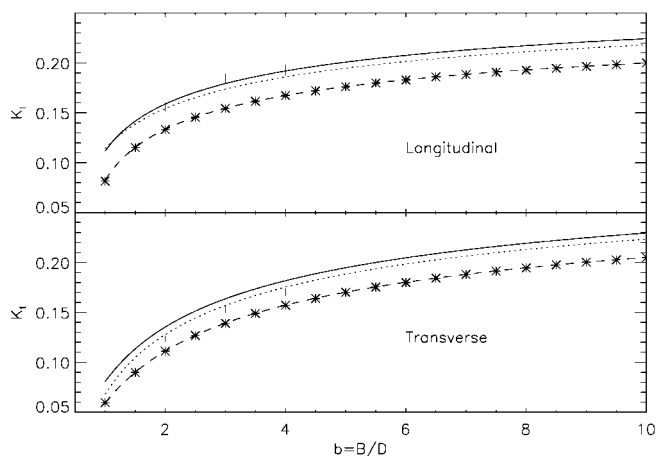


FIG. 3.—Comparison of the coefficients for longitudinal (*top*) and transverse (*bottom*) image motion  $K_l$  and  $K_t$ . *Solid line*: Zernike tilts, eq. (8); *dashed line*: G-tilts, eq. (7); *dotted line*: Sarazin & Roddier (1990) formulae, eq. (6). Asterisks show the results of numerical integration by Martin (1987): data from his Table 2 multiplied by 0.340. Vertical lines are the results of my numerical simulation with windowing centroids and 2000 realizations; bar length reflects the  $\pm 1 \sigma$  statistical error of simulation.

The constant  $K$  depends on the ratio of aperture separation  $B$  to their diameter  $D$ , i.e.,  $b = B/D$ , on the direction of image motion (longitudinal, i.e., parallel to apertures vector, or transverse, i.e., perpendicular), and on the type of tilt considered. The widely used equations (13) and (14) from Sarazin & Roddier (1990) were derived from a crude approximation  $B \gg D$  and imprecise coefficient:

$$\begin{aligned} K'_{lG} &= 0.358(1 - 0.541b^{-1/3}), \\ K'_{tG} &= 0.358(1 - 0.810b^{-1/3}). \end{aligned} \quad (6)$$

*G-tilt.*—Useful formulae for the covariance of the G-tilt were given recently by Conan et al. (2000). I take their main equation (9) for the case  $B > D$  for the covariance, a particular case of their equation (8) for the variance ( $B = 0$ , see also their eq. [27]), and find their difference up to the second term in  $B/D$ . The result is

$$\begin{aligned} K_{lG} &= 0.340(1 - 0.570b^{-1/3} - 0.040b^{-7/3}), \\ K_{tG} &= 0.340(1 - 0.855b^{-1/3} + 0.030b^{-7/3}). \end{aligned} \quad (7)$$

The coefficient 0.340 is also given by a number of other authors (Martin 1987; Tyler 1994). As shown in Figure 3, the new formulae give an excellent match to the exact coefficients computed by Martin (1987) by direct integration.

*Z-tilt.*—The formulae for differential Z-tilt are given in the book by Sasiela (1994) where a convenient series expansion is provided in equation (7.65). Limiting the development to

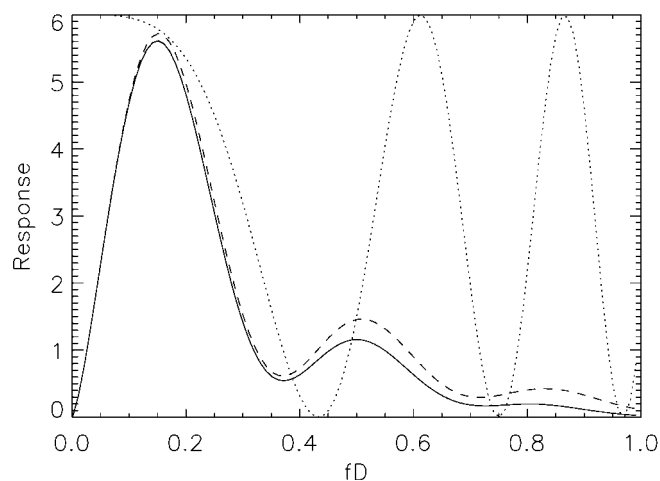


FIG. 4.—Relative contribution of spatial frequencies to the longitudinal differential image motion for G-tilt (*solid line*) and Z-tilt (*dashed line*) according to eqs. (A3) and (A4). The baseline  $B$  is equal to  $3D$  in this example. The maximum contribution comes from spatial periods around  $4D$ – $20D$ . The dotted line shows the additional filter  $F(z, f)$  resulting from the propagation over a distance of 16 km ( $D = 6$  cm,  $\lambda = 0.6 \mu\text{m}$ ) as described in the Appendix, eq. (A5).

two terms in  $b$ ,

$$\begin{aligned} K_{lZ} &= 0.364(1 - 0.532b^{-1/3} - 0.024b^{-7/3}), \\ K_{tZ} &= 0.364(1 - 0.798b^{-1/3} + 0.018b^{-7/3}). \end{aligned} \quad (8)$$

Miraculously, these formulae are closer to the approximate coefficients given by Sarazin & Roddier than to the true coefficients for G-tilt. Equation (8) must be now used to compute seeing from differential image motion, but the difference in coefficients compared to equation (6) is small.

In Figure 3, all three sets of coefficients are plotted for longitudinal and transverse image motion. I also simulated atmospheric wave fronts, computed the variance of spot centroids (with windowing), and compared the results with the formulae to show that the DIMM signal is indeed close to Z-tilt.

### 2.3. DIMM as a Spatial Filter

A DIMM is not sensitive to wave-front perturbations that are either smaller than its apertures or larger than its baseline. Therefore, it acts as a spectral filter and isolates from the turbulence spectrum a particular frequency band. This filtering is slightly different for G- and Z-tilts. In Figure 4, an example of these filters for longitudinal image motion is given. The formulae are given in the Appendix.

It is important to note that the DIMM is insensitive to the low-frequency part of any turbulence spectrum and hence is not affected by the turbulence outer scale. The formulae in Conan et al. (2000) actually include the effects of the turbulence

outer scale  $L_0$ . The most significant correction to  $K_{IG}$  and  $K_{IG}$  is  $\pi D/L_0 \approx 10^{-4}$  for  $L_0 = 20$  m and  $D = 10$  cm, i.e., totally negligible (see also Borgnino, Martin, & Ziad 1992). It means that a DIMM measures the Fried parameter  $r_0$  reliably even for non-Kolmogorov turbulence.

### 3. DEBIASING DIMM DATA

#### 3.1. Noise Bias

Even if the pair of images in a DIMM is absolutely steady (no turbulence), the measured image motion is still not zero because coordinates of the spots are determined with some errors. This *noise variance* adds to the atmospheric image motion variance and makes the apparently measured seeing worse. Here I estimate this bias and propose a cure.

CCDs are most frequently used as image detectors in DIMMs. Their pixels are geometrically very stable: the errors in measured centroids come from the noise in the light intensities: Poisson noise of the signal itself, additive readout noise (RON) of the CCD, and variations of the pixel sensitivity (flat field) that are usually left uncorrected.

Simulations show that in current DIMMs, the rms RON of 10–20 electrons gives the major contribution to the noise variance. Fortunately, this noise component is easy to model for window-limited centroids. Let  $R$  be the rms readout noise and  $I_{\text{tot}}$  be the total flux in the stellar image, both measured in the same units (ADUs or electrons). RON is independent of signal, and a straightforward development of equation (3) leads to the centroid variance:

$$\sigma_R^2 = \frac{R^2}{I_{\text{tot}}^2} \sum_{\text{window}} (x_{ij} - \bar{x})^2. \quad (9)$$

Here  $\sigma_R$  is expressed in CCD pixels and is computed for one spot only;  $2\sigma_R^2$  must be subtracted from the measured variance of differential image motion in a DIMM to remove the bias due to RON. Summation is performed only within the selected window, the average coordinate  $\bar{x}$  is zero if  $x$  is counted from window center. This equation was given by Verin & Muñoz-Tuñón (1995) for the case of a square window; here it is general.

The contribution of RON to the image motion variance is inversely proportional to the *square* of the stellar flux. Thus, going to fainter stars or shortening the exposure time can have a strong effect on this bias. The noise is also proportional to the *fourth* power of window size, which strongly favors selecting the smallest possible window for centering.

A nice feature of equation (9) is that all quantities are either known or easily measurable. Indeed, the sum of square coordinates depends only on the radius of the centering window. RON  $R$  can be measured in ADUs by taking dark frames, subtracting the same bias frame as used for actual spot images, and computing the variance of the resulting frame. Note that  $\sigma_R^2$  does not depend on the shape of the spots!

On the other hand, the *photon-noise variance*  $\sigma_p^2$  does depend

on the size of spots. It is very useful to monitor the optical quality of any DIMM by measuring the Strehl ratio of both spots. If  $I_{\text{max}}$  is the maximum pixel intensity in a spot and  $I_{\text{tot}}$  is the total flux (sum over all pixels), the Strehl ratio  $S$  can be estimated as

$$S = \frac{I_{\text{max}}}{I_{\text{tot}}} \frac{4}{\pi} \left( \frac{\lambda_{\text{CCD}}}{D\Delta x} \right)^2, \quad (10)$$

where  $\Delta x$  is the CCD pixel size in radians, supposed to be much smaller than the Airy spot size. The wavelength  $\lambda_{\text{CCD}}$  here must approximate the maximum CCD sensitivity, e.g.,  $\lambda_{\text{CCD}} = 0.7 \mu\text{m}$ . Ideally, we should obtain  $S = 1$  with good optics; in practice  $S$  is always less than 1 because of finite pixel size, aberrations, etc., and typical empirical values are between 0.4 and 0.7.

The photon noise variance is equal to the second moment of the intensity distribution in the spot  $\zeta^2 = I_{\text{tot}}^{-1} \sum (x_{ij} - \bar{x})^2 I_{ij}$  divided by the total number of photoelectrons in the image  $N$ . The justification for this is simple: 1 photon measures a coordinate with a variance of  $\zeta^2$ ,  $N$  photons improve the result like  $N$  repeated measurements. Practically, a conversion factor from ADUs to electrons must be known to deduce  $N$  from  $I_{\text{tot}}$ . For an ideal Airy spot, the second moment  $\zeta^2$  is infinite, but windowing removes this problem because the sum extends over a limited number of pixels only.

The parameter  $\zeta^2$  can be computed for real spots, but I suggest a simplified approach. If the image shape remains the same while only its size changes,  $\zeta^2$  is proportional to  $S^{-2}$ . With this approximation the photon noise variance for one spot (in square radians) is

$$\sigma_p^2 \approx 0.5 \frac{(0.70\lambda/D)^2}{NS}. \quad (11)$$

The coefficient 0.70 was adjusted from simulations to obtain correct photon noise values with ideal Airy spots and a window of optimum radius. The multiplier 0.5 is not needed for differential variance (two spots).

In Figure 5, the results of DIMM simulations are shown. The CCD pixel size was 0.74, close to typical. The lowest line corresponds to the photon noise alone: even for a third-magnitude star and a relatively small 6 cm aperture,  $\sigma_p$  remains small compared to  $\sigma_R$ . It can be seen that  $\sigma_R$  can be relatively well modeled by equation (9). Noise in the simulations is still a bit higher than the model, presumably because the additional error that comes from window centering is not accounted for by the model.

The third source of noise is the nonuniformity of the CCD sensitivity over the field (flat field). In modern CCDs, the amplitude of sensitivity variations is typically only a few percent. For the actual stellar fluxes, the relative Poisson noise in individual pixels is larger than this, so the flat-field effect can be neglected together with the Poisson noise.

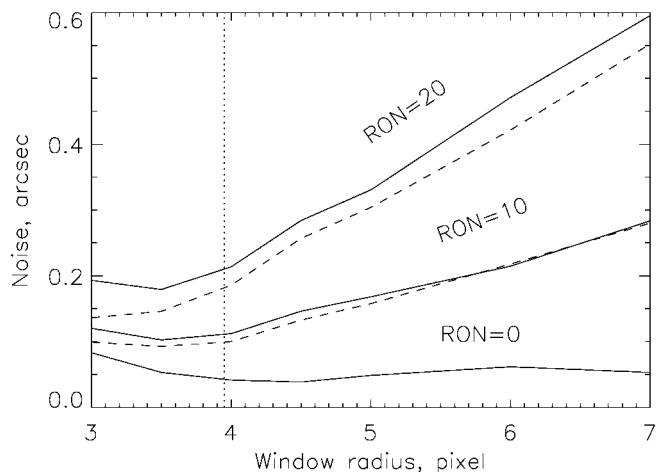


FIG. 5.—rms noise of differential image motion as a function of window radius and rms readout noise RON in electrons. *Solid lines*: Results of simulation for a 3 mag star, 10 ms exposure time,  $D = 6$  cm,  $B = 19.3$  cm. *Dashed lines*: Noise models as a sum of RON = 0 curve and RON contribution from eq. (9). The vertical line marks the optimum window radius of  $1.22\lambda/D$ .

The relative assessment of noise sources is detector-specific. For directly illuminated CCDs, the RON contribution dominates and must be subtracted from the measured variance using equation (9). But in DIMMs with intensified CCDs (Vernin & Muñoz-Tuñón 1995), the RON can be neglected, while Poisson noise and, probably, flat-field noise are the main components.

### 3.2. Exposure Time

The theory of the DIMM presumes that image motion is measured with infinitely short exposures, i.e., the spots are completely “frozen” during the exposures. In reality, DIMMs use a finite exposure time between 5 and 20 ms. The effect is important: for a wind speed of  $40 \text{ m s}^{-1}$  as often found in the upper atmosphere, a turbulent layer moves 40 cm during a 10 ms exposure, considerably averaging the image motion compared to the 10 cm apertures of a typical DIMM. Martin (1987) pointed out the critical role of the exposure time in DIMMs and derived formulae to compute a reduction in image motion variance for G-tilt. The results for Z-tilt should be similar, given the similarity of respective spatial filters (Appendix).

At the majority of sites, the main contribution to seeing comes from the lowest layers with typically slow winds. At such sites, the seeing measured with 10 and 20 ms exposure time would be similar, giving a misleading impression that 10 ms exposure is short enough to freeze image motion. But at some other sites the situation may be different, so a comparison between sites based on exposure-biased seeing can be suspect.

Reduction of image motion variance depends on the relative drag  $V\tau/D$  of a wave front moving with speed  $V$  during exposure time  $\tau$  for aperture diameter  $D$ . It also depends on the baseline

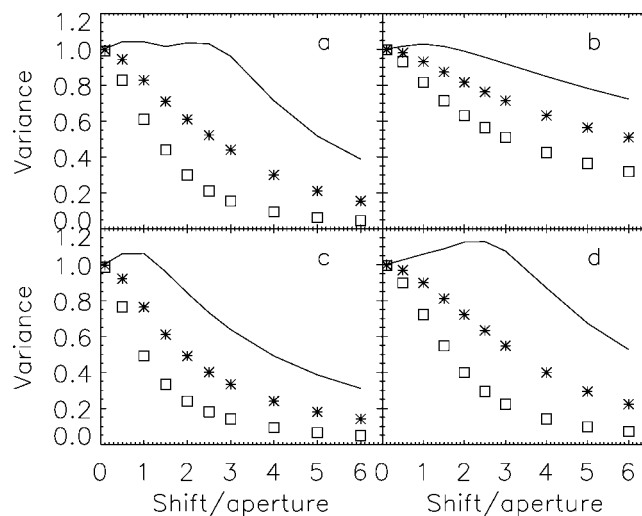


FIG. 6.—Relative attenuation of the variance of differential image motion produced by a single turbulent layer is plotted against the relative aperture shift during exposure  $V\tau/D$  for the case  $B/D = 3$  (*asterisks*). Squares denote the variance attenuation with double exposure. The line depicts the variance corrected by the modified exponential prescription (eq. [12]). The four panels correspond to different combinations of baseline orientation  $\psi$  and wind direction  $\theta$  with respect to the image motion direction: *a*:  $(0^\circ, 0^\circ)$ ; *b*:  $(0^\circ, 90^\circ)$ ; *c*:  $(90^\circ, 0^\circ)$ ; *d*:  $(90^\circ, 90^\circ)$ .

length, on the wind direction relative to the baseline, and on which component of image motion (longitudinal or transverse) is measured. Less reduction is experienced by the longitudinal component for the wind direction perpendicular to the baseline. Thus, a north-south baseline orientation is recommended because westerly winds in the high atmosphere are predominant at midlatitude sites.

If we are not able to reduce the exposure time to that needed to freeze the seeing, we can take data with double exposures to control this effect and, hopefully, to correct it. This is the idea of *interlaced exposures* as implemented in some DIMMs (Sarazin 1997). Let  $\epsilon_1$  be the seeing measured with some exposure time  $\tau$ , and  $\epsilon_2$  be the seeing with double the exposure time  $2\tau$ . Long and short exposures are interlaced so that data are not affected by seeing variations.

If the measured seeing decays with exposure time exponentially, as  $\exp(-a\tau)$ , then the correct (zero-exposure) seeing would be obtained by multiplication of  $\epsilon_1$  by  $\epsilon_1/\epsilon_2$ . This correction can be applied to image motion variance instead of seeing with the same result. I found that this prescription often “overshoots” and propose a milder “modified exponential” correction law:

$$\epsilon_{\text{corr}} = \epsilon_1^{1.75} \epsilon_2^{-0.75}. \quad (12)$$

The actual dependence of variance attenuation on exposure time is not exponential, so the correction can be only approximate. How good is it? In Figure 6, the attenuation of variance

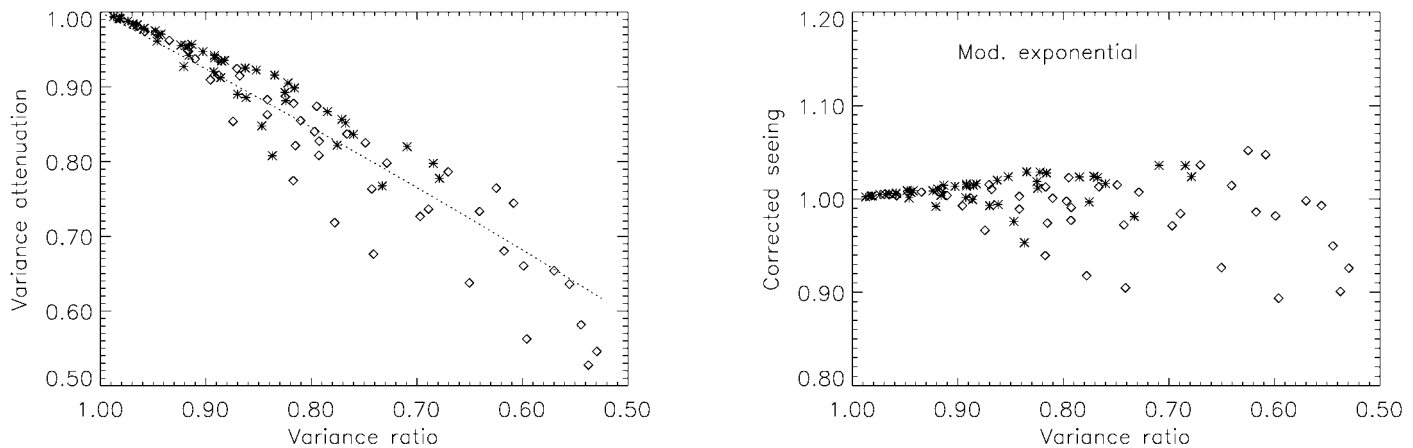


FIG. 7.—*Left*: Attenuation of the differential image motion variance due to the finite exposure time  $\tau$  is plotted against the ratio of image motion variance measured with  $2\tau$  and  $\tau$ . *Asterisks*:  $\tau = 5$  ms; *diamonds*:  $\tau = 10$  ms. All four combinations of directions are plotted jointly for the 11 profiles, giving 44 points for each exposure. The dotted line shows the general trend. *Right*: Ratio of seeing corrected with modified exponential prescription to the true seeing for pairs of 5 and 10 ms exposures (*asterisks*) and 10 and 20 ms exposures (*diamonds*).

with single and double exposure time for baseline  $B = 3D$  is plotted as a function of relative shift  $V\tau/D$ . The calculations were done by computing the integral in equation (14) of Martin (1987). The line shows the corrected variance according to the prescription in equation (12). Much of the exposure-time effect is removed, with small overcorrection at low wind speed and undercorrection at high wind speed.

Terrestrial atmosphere is a collection of turbulent layers moving with different speeds in different directions. Calculations such as those in Figure 6 should be repeated for each layer and then averaged with weights proportional to the turbulence strength in each layer. I performed such calculations for 11 profiles of turbulence and wind speed measured at Cerro Paranal (Chile) in 1992 during the PARSCA campaign (Fuchs & Vermin 1996). Wind direction is not known, so I assumed that all layers move in the same direction, which was taken to be either parallel or perpendicular to the baseline. For each wind direction, the attenuation of longitudinal and transverse variance was computed, so 11 profiles provided a total of 44 variance estimates for each exposure. I adopted DIMM parameters  $D = 6$  cm and  $B = 19$  cm and computed the variance attenuation for exposure times of 5, 10, and 20 ms. The results are shown in Figure 7.

It is evident from Figure 7 that uncorrected seeing can be severely biased. In the worst case, the “10 ms” variance is only  $\frac{1}{2}$  of its true value. Even 5 ms is not short enough if seeing is to be measured to better than 10%. Most of this bias can be removed with modified exponential correction; the remaining error in seeing is under 5% in most cases and, moreover, is no longer systematic. *If Paranal profiles are representative of good astronomical sites, these calculations validate the interlaced-exposure technique.*

There are, however, two problems with this method. First, at shorter exposures, the bias in variance caused by the RON is 4 times larger than at longer exposures, being inversely pro-

portional to the square of stellar flux. If this effect is not taken into account, the increase of the variance at shorter exposures is erroneously taken as being of atmospheric origin and provokes overcorrection. Subtraction of noise variance is mandatory for the interlaced-exposure technique to work.

The second problem concerns low accuracy of seeing values obtained by the interlaced-exposure technique. If the seeing is stationary during accumulation of image-motion variance, the variance is measured with a relative rms error of  $M^{-1/2}$  and the seeing (variance to the power 0.6; eq. [5]) with a relative error of  $0.6M^{-1/2}$ , where  $M$  is the number of data points (spot images). During 1 minute, some  $M = 6000$  10 ms exposures can be taken, but in practice only  $M \sim 300$  can be achieved because the CCD readout rate limits the data flow. With the interlaced-exposure technique, we reduce  $M$  twice and further amplify the variance of measured seeing by  $1.75^2 + 0.75^2 = 3.625$  times when applying equation (12). Thus, corrected seeing is now measured with a relative rms error of  $0.6 [(2 \times 3.625)/M]^{1/2}$ , which increases 2.7 times as a result of interlaced-exposure correction.

The loss of statistical accuracy can be avoided by a more reasonable strategy, however. Wind structure in the atmosphere changes only slowly, on a timescale of hours. The seeing bias must also change slowly, permitting some averaging. Let  $c_1 = (\epsilon_1/\epsilon_2)^{0.75}$  be the correction factor needed to obtain zero-exposure seeing  $\epsilon_0$  from  $\epsilon_1$  according to equation (12). Then the correction factor for double-exposure seeing would be  $c_2 = c_1\epsilon_1/\epsilon_2 = c_1^{1.75}$ . Now we can combine both short- and long-exposure data in a final corrected seeing estimate:

$$\epsilon_0 = 0.5(c_1\epsilon_1 + c_1^{1.75}\epsilon_2). \quad (13)$$

Smoothing of  $c_1$  over time can be done by any technique, e.g., by running-box average. Archival seeing data that contain both  $\epsilon_1$  and  $\epsilon_2$  can be reprocessed in order to obtain better (less

noisy) seeing statistics. For real-time DIMM data processing, I suggest to average the correction factors recursively. Some initial guess for  $c_1$  is used at the start of the night. When new data arrive, we compute the instantaneous correction  $c'_1 = (\epsilon_1/\epsilon_2)^{0.75}$ , but instead of applying it directly to the data, we only adjust the average correction recursively:

$$c_1^{\text{new}} = (1 - g)c_1^{\text{current}} + gc'_1. \quad (14)$$

With a reasonably small gain, e.g.,  $g = 0.05$ , the system would average the corrections over  $\sim g^{-1} = 20$  data points and thus would be able to track the variations in the seeing “speed” without noise penalty.

## 4. SEEING IN LARGE TELESCOPES: THE INFLUENCE OF OUTER SCALE

### 4.1. Kolmogorov Model

Suppose that the parameter  $r_0$  is measured correctly by a DIMM. How can it be used to predict the size of long-exposure seeing-limited images in large ( $D \gg r_0$ ) telescopes?

The standard theory based on the Kolmogorov turbulence model (Roddier 1981) leads to a relation between  $r_0$ , the phase structure function  $D_\phi(\mathbf{r})$ , and the optical transfer function (OTF)  $T_0(\mathbf{f})$  of a large telescope:

$$D_\phi(\mathbf{r}) = 6.88(|\mathbf{r}|/r_0)^{5/3}, \quad (15)$$

$$T_0(\mathbf{f}) = \exp[-0.5D_\phi(\lambda\mathbf{f})], \quad (16)$$

where  $\mathbf{f}$  is the spatial frequency (in inverse radians) and  $\lambda$  is the imaging wavelength. The corresponding atmospheric PSF is obtained from the OTF by a Fourier transform (FT). There is no analytic expression: the PSF must be computed numerically. The FWHM of the atmospheric PSF  $\epsilon_0$  is given by equation (5). Similarly, the diameter of the circle that contains one-half of the total PSF energy (full width at half-energy, sometimes also called d50)  $\beta_0$  is found to be

$$\beta_0 = 1.15\lambda/r_0. \quad (17)$$

### 4.2. von Kármán Model

The von Kármán turbulence model introduces an additional parameter, the wave-front outer scale  $L_0$  (Borignino 1990; Ziad et al. 2000). Physically, the outer scale is related to the largest size perturbations, but the “geophysical” local turbulence outer scale  $L_0$  should not be confused with the optical parameter  $L_0$  that describes wave-front statistics after propagation through the whole atmosphere. Nobody has actually verified this model, but it gives a better description of wave-front statistics at scales of a few meters than the standard model. Typical values of  $L_0$  are around 20 m, with a scatter from  $\sim 10$  m to few hundred meters (Ziad et al. 2000);  $L_0$  does not depend on wavelength.

The analytic expression for the phase structure function

in the von Kármán model can be found in (Conan 2000; Consortini & Ronchi 1972)

$$D_\phi(r) = \frac{\Gamma(11/6)}{2^{11/6}\pi^{8/3}} \left[ \frac{24}{5} \Gamma\left(\frac{6}{5}\right) \right]^{5/6} \left( \frac{r_0}{L_0} \right)^{-5/3} \times \left[ 2^{-1/6} \Gamma\left(\frac{5}{6}\right) - \left( \frac{2\pi r}{L_0} \right)^{5/6} K_{5/6}\left( \frac{2\pi r}{L_0} \right) \right], \quad (18)$$

where  $K_{5/6}(x)$  is the modified Bessel function of the third kind, or McDonald function, and  $\Gamma(x)$  is the gamma function. The corresponding OTF  $T_{\text{vK}}(\mathbf{f})$  is obtained from equation (16). In the limit  $L_0 = \infty$  (Kolmogorov model), equation (18) transforms to equation (15).

The FT of  $T_{\text{vK}}(\mathbf{f})$  formally does not exist because at large  $\mathbf{f}$ , the OTF does not go to zero [ $D_\phi(r)$  saturates]. It means that there remains some coherence of wave fronts at large baselines, and in an infinitely large telescope the PSF will contain a delta function at its center. In a telescope of finite size, the central core will be diffraction-limited. Of course, this situation is not physical, and such coherent cores in seeing-limited images were never observed, despite a lone voice to the contrary (Griffin 1973). See also the dispute between McKechnie (1992) and Tatarskii & Zavorotny (1993) on this topic.

To circumvent the mathematical difficulties, I subtract from  $T_{\text{vK}}(\mathbf{f})$  the (small) constant level that it reaches at the limit of the computing grid, renormalize the remaining OTF, and take the FT. The result should be a good approximation to the seeing-limited PSF in large telescopes (it does not depend on telescope diameter, like in the case of Kolmogorov model). The effect of finite  $L_0$  can be understood as an increase of wave-front coherence at small baselines.

The FWHM and half-energy diameter of the von Kármán PSF were computed as a function of  $L_0/r_0$ . With good seeing ( $r_0 = 15$  cm at  $0.5 \mu\text{m}$ ) and a typical  $L_0 = 20$  m,  $L_0/r_0 = 133$  at  $\lambda = 0.5 \mu\text{m}$  and  $L_0/r_0 = 22$  at  $2.2 \mu\text{m}$ . Compared to the standard theory, the FWHM  $\epsilon_{\text{vK}}$  is reduced by 21% in the visible and by 1.9 times at  $2.2 \mu\text{m}$ —quite a difference! The “improvement” of the half-energy diameter  $\beta_{\text{vK}}$  is less significant.

A rough idea about the effect of outer scale can be obtained if one presumes that the image motion is greatly reduced for finite  $L_0$ . Of course, the amount of image motion depends on the telescope diameter, hence it is system-dependent, whereas the image improvement is not. Still, I can model the effect as a quadratic subtraction of some component from the image width. This leads to an approximation

$$\left( \frac{\epsilon_{\text{vK}}}{\epsilon_0} \right)^2 \approx 1 - 2.183 \left( \frac{r_0}{L_0} \right)^{0.356}, \quad (19)$$

which was obtained by fitting to the numerical results. This approximation turns out to be very good, with relative errors within  $\pm 1\%$  for  $L_0/r_0 > 20$ . A similar formula for half-energy

diameter  $\beta_{\text{vK}}$  is good to  $\pm 1\%$  for  $L_0/r_0 > 10$ :

$$\left(\frac{\beta_{\text{vK}}}{\beta_0}\right)^2 \approx 1 - 1.534 \left(\frac{r_0}{L_0}\right)^{0.347}. \quad (20)$$

When  $r_0$  measured by a DIMM is used to predict image size in large telescopes, the effects of outer scale are significant in the visible range and much more so in the infrared. The spatial spectrum of a wave front is most certainly different from the von Kármán model, so the equations (19) and (20) should be considered as only first-order approximations to reality. Still, this approximation is better than the standard infinite-scale theory.

Equations (19) and (20) should *not* be used to convert DIMM data into seeing because they contain an additional parameter  $L_0$ . Instead, knowing the DIMM seeing as defined above and the wavelength of observations, the image size in large telescopes can be predicted using these relations and adopting some plausible values for  $L_0$ .

Unlike the DIMM, some seeing-measuring techniques (interferometer or absolute image motion) are sensitive to outer-scale effects. If the results of these techniques are interpreted in the framework of the standard Kolmogorov model, a better prediction of seeing in large telescopes might result. Unfortunately, all these methods are sensitive to telescope pointing errors and for this reason are not practical.

## 5. CONCLUSIONS AND RECOMMENDATIONS

The aim of this paper is to clarify various aspects of the—now standard—seeing measuring technique using the DIMM. The first point is that the interpretation of DIMM data as seeing is not trivial. Differences between DIMM seeing and image size in large telescopes are to be expected, especially in the infrared, because turbulence does not entirely conform to the standard infinite-scale model. What the DIMM really measures is the Fried parameter  $r_0$ , which is traditionally expressed in terms of seeing. Keeping in line with this tradition, I suggest to use always one and the same equation (5) for a standard wavelength of  $0.5 \mu\text{m}$  in order to make the conversion of seeing back to  $r_0$  possible.

The second important conclusion is that several instrumental effects can bias DIMM data in a systematic way. Table 1 summarizes these biases. None of them has a dramatic influence on the measured seeing (except CCD noise under some unfavorable circumstances).

The last two effects in Table 1 are not very important, but still deserve mentioning. Propagation along a distance  $z$  reduces the image motion for the layers that are in the “far field” for DIMM apertures [ $D \leq (\lambda z)^{1/2}$ ]. This leads to some underestimation of any high-layer contribution to seeing (Appendix). The influence of outer scale can be totally neglected: a DIMM measures the Fried parameter  $r_0$  reliably even for non-Kolmogorov turbulence.

TABLE 1  
BIASES IN DIMM DATA

Effect	Seeing Bias	Typical Effect (%)
Thresholding .....	Decrease	~9
RON in CCD .....	Increase	0–100
Finite exposure .....	Decrease	10–20
Near-field approximation .....	Decrease	<10
Outer scale .....	Negligible	<1

In most of the currently working DIMMs, these effects are usually neglected. Some partial compensation of biases may occur, however. When DIMM seeing is compared to the telescope seeing, the latter is also biased: increased by turbulence inside the dome and decreased by outer-scale effect. An agreement between DIMM and telescope seeing to better than 10% may thus be fortuitous.

The methods to take into account the two most important biases (finite exposure time and noise) are proposed here and studied by means of numerical modeling. The following recommendations for DIMM designers and users can be formulated as a result of the present work:

1. Make the DIMM apertures and baseline as large as feasible. It reduces both exposure time effects and noise bias.
2. Control the optical quality of DIMM by computing and archiving the Strehl ratio (eq. [10]).
3. Use a centroiding algorithm with a window radius of  $1.22\lambda/D$  or slightly larger.
4. Measure the readout noise of the CCD and subtract the noise variance from the measured image motion variance according to equation (9).
5. Use as short an exposure time as allowed by the hardware and noise. If this exposure is still not short enough, debias the data with the interlaced-exposure technique. In doing this, average the correction factors (eqs. [12] and [14]) to avoid the loss of accuracy.
6. Use the correct coefficients (eq. [8]) to derive  $r_0$  from image motion. Always compute  $r_0$  and seeing (eq. [5]) for a standard wavelength of  $0.5 \mu\text{m}$  and at zenith.
7. Use equation (19) to predict image size in large telescopes.

It is true that DIMM is a simple and robust method to measure the seeing. However, achieving an absolute accuracy of 10% or better requires particular care. I hope that this work will help to better calibrate DIMM data and thus to increase their value.

This work was stimulated by M. Sarazin during numerous and fruitful discussions with the author. Some ideas were implemented and tested at the CTIO DIMM jointly with E. Bustos, H. E. Schwarz, and M. Boccas. S. Baumont and H. E. S. have kindly checked the manuscript and formulae.

## APPENDIX

## SPATIAL FREQUENCY FILTERING IN DIMMs

The response of DIMMs to wave-front corrugations of different spatial scales is considered here. For G-tilt, the filter in frequency space includes the gradient operator along the  $x$ -axis,  $-2\pi if_x$ , the factor  $\lambda/(2\pi)$  to convert it to angles, the aperture averaging factor  $2J_1(\pi Df)/(\pi Df)$ , and the “difference” operator corresponding to the two DIMM apertures. The latter is an FT of the sum of two delta functions with opposite signs displaced by  $B/2$  and  $-B/2$  from coordinate origin and is equal to  $2 \sin(\pi f_x B)$ . Thus, the spectral filter  $F_G$  is equal to

$$F_G = -if_x \lambda \frac{2J_1(\pi Df)}{\pi Df} \sin(\pi f_x B). \quad (\text{A1})$$

Here  $f = |f|$ , where  $f$  is the spatial frequency vector with components  $f_x, f_y$ .

For differential Z-tilt, we have to replace the combination of gradient and aperture averaging with the Fourier transform of the Zernike polynomial number 2 (tilt along the  $x$ -axis),  $4f_x J_2(\pi Df)/(\pi f^2 D)$ . A factor  $2\lambda/(\pi D)$  must again be introduced to pass from Zernike amplitude to angle. The term corresponding to the difference between two apertures remains the same. Thus,

$$F_Z = 8f_x \frac{\lambda}{\pi D} \frac{J_2(\pi Df)}{\pi f^2 D} \sin(\pi f_x B). \quad (\text{A2})$$

Variance of differential image motion is computed as an integral over spatial frequencies of the product of the filter square modulus  $|F|^2$  and the turbulence power spectrum, which is proportional to  $f^{-11/3}$  for the Kolmogorov turbulence model. I omit wavelength and other proportionality terms to underline the difference between the two tilts. Integration over angle in frequency plane can be done analytically (cf. eq. [13] in Martin 1987), leaving only the integration over the modulus of the frequency. Usually the dimensionless frequency  $q = Df$  is used. I considered above only the longitudinal image motion ( $\psi = 0$ ); for an arbitrary direction  $\psi$ , the integrand  $I_G$  for G-tilt looks like

$$I_G(q) = q^{-2/3} \left[ \frac{2J_1(\pi q)}{\pi q} \right]^2 \left[ 1 - 2 \cos^2 \psi J_0(2\pi b q) + \cos(2\psi) \frac{2J_1(2\pi b q)}{2\pi b q} \right], \quad (\text{A3})$$

while for Z-tilt the integrand has the form

$$I_Z(q) = 64q^{-2/3} \left[ \frac{J_2(\pi q)}{\pi^2 q^2} \right]^2 \left[ 1 - 2 \cos^2 \psi J_0(2\pi b q) + \cos(2\psi) \frac{2J_1(2\pi b q)}{2\pi b q} \right]. \quad (\text{A4})$$

Comparison of  $I_G$  and  $I_Z$  gives a clear idea on the relative contribution of different spatial frequencies to the differential image motion (Fig. 4). Z-tilt contains somewhat more higher frequency power and hence can be more affected by finite exposure time than G-tilt.

Additional spectral filtering comes from the propagation: diffraction converts part of turbulent energy into scintillation, with phase fluctuations and image motion correspondingly reduced. Maximum reduction does not exceed a factor of 2, however. Given the distance to the layer,  $z$ , the integrand must be multiplied by the additional diffraction term  $F(z, f)$ :

$$F(z, f) = \cos^2(\pi \lambda z f^2). \quad (\text{A5})$$

In Figure 4, this term is overplotted for the worst-case situation of a high layer and small DIMM apertures. In this case, longitudinal image motion variance is 0.76 times that of a low layer of the same intensity. Increasing the aperture size to 10 cm brings the reduction factor to 0.83, which still corresponds to an 11% bias on seeing. Fortunately, turbulence in the upper atmosphere seldom dominates the overall integral, so this effect for realistic turbulence profiles will be almost negligible.

## REFERENCES

- Andersen, T., Ardeberg, A., & Gilmozzi, R., eds. 1999, ESO Conf. and Workshop Proc. 57, Backaskog Workshop on Extremely Large Telescopes (Garching: ESO)
- Borgnino, J. 1990, *Appl. Opt.*, 29, 1863
- Borgnino, J., Martin, F., & Ziad, A. 1992, *Opt. Commun.*, 91, 267
- Conan, R. 2000, Ph.D. thesis, Nice Univ.
- Conan, R., Borgnino, J., Ziad, A., & Martin, F. 2000, *J. Opt. Soc. Am. A*, 17, 1807
- Consortini, A., & Ronchi, L. 1972, *Appl. Opt.*, 11, 1205
- Dainty, J. C., & Scaddan, R. J. 1975, *MNRAS*, 170, 519
- Ehgamberdiev, S. A., et al. 2000, *A&AS*, 145, 293
- Fried, D. 1965, *J. Opt. Soc. Am.*, 55, 1427
- . 1975, *Radio Sci.*, 10, 71
- Fuchs, A., & Vernin, J. 1996, Final Report on PARSCA 1992 and 1993 Campaigns (ESO Tech. Rep. VLT-TRE-UNI-17400-001; Garching: ESO)
- Griffin, R. F. 1973, *Observatory*, 93, 3
- Irwan, R., & Lane, R. G. 1999, *Appl. Opt.*, 38, 6737
- Martin, H. M. 1987, *PASP*, 99, 1360
- McKechnie, T. S. 1992, *J. Opt. Soc. Am. A*, 9, 2415
- Roddier, C. 1976, *J. Opt. Soc. Am.*, 66, 478
- Roddier, F. 1981, in *Progress in Optics*, ed. E. Wolf (Amsterdam: North-Holland), 281
- Roddier, F., Graves, J. E., & Limburg, E. 1990, *Proc. SPIE*, 1236, 474
- Sagar, R., et al. 2000, *A&AS*, 144, 349
- Sarazin, M. 1997, *Proc. SPIE*, 3125, 367
- Sarazin, M., & Roddier, F. 1990, *A&A*, 227, 294
- Sasiela, R. J. 1994, *Electromagnetic Wave Propagation in Turbulence* (Berlin: Springer)
- Stock, J., & Keller, G. 1960, in *Stars and Stellar Systems*, Vol. 1, Telescopes, ed. G. P. Kuiper & B. M. Middlehurst (Chicago: Univ. Chicago Press), 138
- Tatarskii, V. I. 1961, *Wave Propagation in a Turbulent Medium* (New York: Dover)
- Tatarskii, V. I., & Zavorotny, V. J. 1993, *J. Opt. Soc. Am. A*, 10, 2410
- Tyler, G. 1994, *J. Opt. Soc. Am. A*, 11, 358
- van Dam, M. A., & Lane, R. G. 2000, *J. Opt. Soc. Am. A*, 17, 1319
- Vernin, J., & Muñoz-Tuñón, C. 1995, *PASP*, 107, 265
- Wang, J. Y., & Markey, J. K. 1978, *J. Opt. Soc. Am. A*, 68, 78
- Wood, P. R., Rodgers, A. W., & Russell, K. S. 1995, *Publ. Astron. Soc. Australia*, 12, 97
- Young, A. 1974, *ApJ*, 189, 587
- Ziad, A., et al. 2000, *Appl. Opt.*, 39, 5415